New quadratic solid-shell elements and their evaluation on popular benchmark problems

Farid Abed-Meraim, Vuong-Dieu Trinh, Alain Combescure

New quadratic solid–shell elements and their evaluation on linear benchmark problems

Farid Abed-Meraim · Vuong-Dieu Trinh · Alain Combescure

Abstract This paper is concerned with the development of a new family of solid–shell finite elements. This concept of solid–shell elements is shown to have a number of attractive computational properties as compared to conventional three-dimensional elements. More specifically, two new solid–shell elements are formulated in this work (a fifteen-node and a twenty-node element) on the basis of a purely three-dimensional approach. The performance of these elements is shown through the analysis of various structural problems. Note that one of their main advantages is to allow complex structural shapes to be simulated without classical problems of connecting zones meshed with different element types. These solid–shell elements have a special direction denoted as the "thickness", along which a set of integration points are located. Reduced integration is also used to prevent some locking phenomena and to increase computational efficiency. Focus will be placed here on linear benchmark problems, where it is shown that these solid–shell elements perform much better than their counterparts, conventional solid elements.

F. Abed-Meraim (✉)
Laboratoire d'Études des Microstructures et de Mécanique des Matériaux,
UMR CNRS 7239, Arts et Métiers ParisTech, 4 rue Augustin Fresnel,
57078 Metz Cedex 03, France
e-mail: farid.abed-meraim@ensam.eu

V.-D. Trinh
Laboratoire de Mécanique des Structures Industrielles Durables,
UMR EDF/CNRS/CEA 8193, EDF R&D, 1 avenue du Général de Gaulle,
92141 Clamart Cedex, France

A. Combescure
Laboratoire de Mécanique des Contacts et des Structures,
UMR CNRS 5259, INSA de Lyon, Bâtiment Jean d'Alembert,
18-20 rue des Sciences, 69621 Villeurbanne Cedex, France

Keywords Solid–shell finite elements · Mixed variational principle · Locking phenomena · Reduced integration · Rank deficiency · Benchmark problems

1 Introduction

Nowadays, the numerical simulation at various scales has become widespread in the industry, and concerns practically all key sectors (civil engineering, nuclear, aerospace, automotive, packaging, etc). In computational mechanics, the most adopted approach is certainly the finite element method. Despite the important progress achieved in terms of computer resources, a number of nonlinear three-dimensional (3D) problems still require long hours of calculation times. In this context, the efficiency of finite elements becomes of crucial importance to speed up the design processes, for example, or to reduce the simulation costs in general.

Over the past three decades, considerable effort has been devoted to the development of efficient and reliable finite elements. In this regard, reduced-integration elements have been developed for the efficient treatment of general continuum mechanics problems (see, e.g., [1–9]). Concurrently, for structural applications, a variety of efficient plate and shell elements have been proposed on the basis of mixed formulations or using enhanced assumed strain (EAS) methods in order to avoid locking phenomena (see, e.g., [10–17]).

However, in real-life structures, coexistence of 3D zones with structural components is very common, and both types of finite element technologies often need to be simultaneously used. Therefore, finite elements that are effective in both thin structure simulation and general 3D applications would considerably simplify the modeling of such combined structures. Indeed, they would avoid arbitrary definitions of separation zones between bulk and structural components, as well as the intricacies related to the connection of different element types (e.g., solid and structural elements).

In addition, 3D element formulations have many other advantages: they avoid resorting to complex shell kinematics, they use general fully 3D constitutive laws, they allow evaluation of thickness variation through the calculation of strain components in that direction, they enable an easier treatment for large rotations and the corresponding configuration update, they make it automatic the connection between solid and structural elements since the displacements are the only degrees of freedom, and allow natural contact conditions on both sides of the structure.

Consequently, significant attention has been paid to the development of a new concept of solid–shell elements, specifically dedicated to the modeling of thin structures (see [18–26]). Most of the methods previously developed were based on enhanced assumed strain fields, and consisted of either the use of a conventional integration rule with appropriate treatment for locking phenomena, or the adoption of a reduced-integration scheme with effective control of zero-energy (hourglass) modes. Both approaches have been extensively investigated and evaluated through a variety of structural applications, as reported in [6,27–30].

A first solid–shell element that we have developed, based on some relatively simple principles, is an eight-node hexahedron denoted as SHB8PS [21,31]. This concept

aims to combine in a single formulation the well-recognized 3D element advantages with several useful shell features. The evaluation of this element on a variety of benchmark problems confirmed its good performance in terms of accuracy and convergence properties, while using only a single element layer along the thickness. However, with the advent of free mesh generation tools that do not only generate hexahedrons and in order to automatically mesh arbitrarily complex geometries, the development of prismatic solid–shell elements has been made necessary. To this end, a six-node prismatic solid–shell designated as SHB6 has been proposed [32]. Although playing a useful role as a complement to the SHB8PS, the SHB6 element exhibits some shear and thickness-type locking, which is common in linear triangular elements where the strain is constant. The latter limitation represents one of the main motivations behind the current development of alternative complementary solid–shell elements. These proposed elements have quadratic interpolation with both versions, hexahedral and prismatic.

The remaining of the paper is outlined as follows. In Sect. 2, the formulation of the proposed quadratic solid–shell elements, denoted as SHB15 and SHB20, is detailed. In these derivations, the common aspects of the two formulations are emphasized whenever possible. In Sect. 3, the resulting elements are evaluated on a set of selective and representative benchmark problems. Finally, some concluding remarks are drawn in Sect. 4.

2 Formulation of the SHB15 and SHB20 solid–shells

In this section, the formulation of the quadratic solid–shell finite elements SHB15 and SHB20 is detailed. Because the adopted approach has a number of similarities for the two elements, both formulations are conjointly presented to avoid repeating the common aspects.

2.1 Kinematics and interpolation

The SHB15 and SHB20 denote a fifteen-node prismatic element and a twenty-node hexahedral element, respectively. Based on a 3D approach, they have only three displacement degrees of freedom per node. However, a special direction is chosen, designated as the "thickness", normal to the mean plane of these elements. Also, an in-plane reduced-integration rule is used with $3 \times n_{\text{int}}$ and $4 \times n_{\text{int}}$ integration points for the SHB15 and SHB20, respectively. In other words, the in-plane integration employs only 3 points for the SHB15 and 4 for the SHB20, while the number of through-thickness integration points is n_{int}. Similarly to their linear counterparts SHB8PS and SHB6 [31,32], n_{int} is a user-defined number, taken equal to two in elasticity and five in plasticity (see Fig. 1).

Note that the integration points for the SHB15 are located along three lines of respective equations: $(\xi = 1/2, \eta = 1/2)$, $(\xi = 0, \eta = 1/2)$, and $(\xi = 1/2, \eta = 0)$, whereas for the SHB20, they are located along the four lines: $(\xi = -1/\sqrt{3}, \eta = -1/\sqrt{3})$, $(\xi = 1/\sqrt{3}, \eta = -1/\sqrt{3})$, $(\xi = 1/\sqrt{3}, \eta = 1/\sqrt{3})$, and $(\xi = -1/\sqrt{3}, \eta = 1/\sqrt{3})$. The

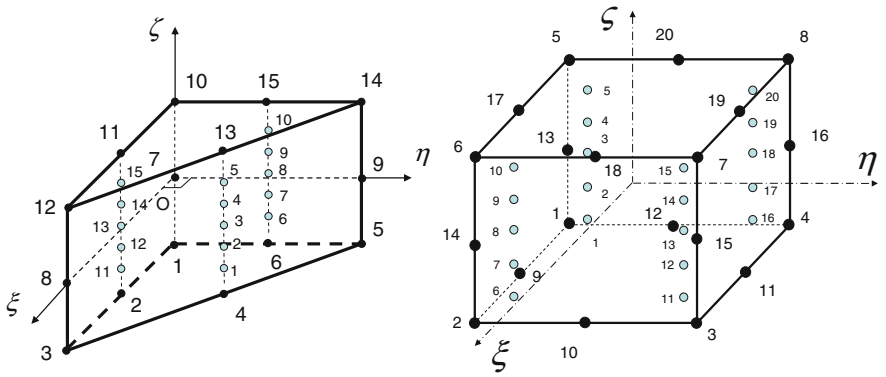

Fig. 1 Reference geometry for the SHB15 and SHB20 and location of integration points ($n_{\text{int}} = 5$)

coordinates of the Gauss points along axis ζ and the associated weights are given in [33] for the SHB15 and SHB20 for both cases: $n_{\text{int}} = 2$ and $n_{\text{int}} = 5$.

Within these two isoparametric elements, the spatial coordinates x_i and displacement field components u_i are related to the nodal coordinates x_{iI} and nodal displacements u_{iI}, respectively, using the quadratic shape functions N_I as

$$x_i = x_{iI} N_I(\xi, \eta, \zeta), \quad u_i = u_{iI} N_I(\xi, \eta, \zeta). \tag{1}$$

In the equation above and hereafter, unless specified otherwise, the implied convention of summation over repeated indices will be followed. Lowercase subscripts i vary from 1 to 3 and represent the spatial coordinate directions, while uppercase subscripts I vary from 1 to 15 for the SHB15 and from 1 to 20 for the SHB20 and correspond to the element nodes. The explicit expressions of the classical quadratic shape functions N_I, corresponding to each of the elements SHB15 and SHB20, can be found for instance in [33].

2.2 Discrete gradient operator

The interpolation of the displacement field, Eq. (1), will allow us to define the strain field and to express the relationships relating the strain field to the nodal displacements. By differentiating (1), the linear strain tensor is written as

$$\varepsilon_{ij} = \frac{1}{2}\left(u_{i,j} + u_{j,i}\right) = \frac{1}{2}\left(u_{iI} N_{I,j} + u_{jI} N_{I,i}\right).$$

Combining Eq. (1) with the expressions of the shape functions leads to the expansion of the displacement field in the form of a constant term, linear terms in x_i, and nonlinear terms involving functions h_α, with ($\alpha = 1, \ldots, 11$) for the SHB15, and ($\alpha = 1, \ldots, 16$) for the SHB20. For the SHB15 element, this expansion reads

$$\begin{cases} u_i = a_{0i} + a_{1i}x_1 + a_{2i}x_2 + a_{3i}x_3 + c_{1i}h_1 + c_{2i}h_2 + c_{3i}h_3 + c_{4i}h_4 \\ \qquad + c_{5i}h_5 + c_{6i}h_6 + c_{7i}h_7 + c_{8i}h_8 + c_{9i}h_9 + c_{10i}h_{10} + c_{11i}h_{11} \\ h_1 = \xi\zeta,\ h_2 = \eta\zeta,\ h_3 = \xi\eta,\ h_4 = \xi\eta\zeta,\ h_5 = \xi^2,\ h_6 = \eta^2, \\ h_7 = \zeta^2,\ h_8 = \xi^2\zeta,\ h_9 = \eta^2\zeta,\ h_{10} = \xi\zeta^2,\ h_{11} = \eta\zeta^2 \end{cases}, \quad i = 1, 2, 3. \tag{2}$$

Evaluating the above equation at the SHB15 element nodes leads to the following three fifteen-equation systems:

$$\begin{cases} \mathbf{d}_i = a_{0i}\mathbf{s} + a_{1i}\mathbf{x}_1 + a_{2i}\mathbf{x}_2 + a_{3i}\mathbf{x}_3 + c_{1i}\mathbf{h}_1 + c_{2i}\mathbf{h}_2 + c_{3i}\mathbf{h}_3 + c_{4i}\mathbf{h}_4 \\ \qquad + c_{5i}\mathbf{h}_5 + c_{6i}\mathbf{h}_6 + c_{7i}\mathbf{h}_7 + c_{8i}\mathbf{h}_8 + c_{9i}\mathbf{h}_9 + c_{10i}\mathbf{h}_{10} + c_{11i}\mathbf{h}_{11} \end{cases}, \quad i = 1, 2, 3 \tag{3}$$

where the fifteen-component vectors $\mathbf{d}_i$ and $\mathbf{x}_i$ represent the nodal displacements and nodal coordinates, respectively, and are defined as

$$\mathbf{d}_i^T = (u_{i1}, u_{i2}, u_{i3}, \ldots.., u_{i15}), \quad \mathbf{x}_i^T = (x_{i1}, x_{i2}, \quad x_{i3}, \ldots.., x_{i15}),$$

while $\mathbf{s}$ and $\mathbf{h}_\alpha$ $(\alpha = 1, \ldots, 11)$ are constant vectors given by

$$\begin{cases} \mathbf{s}^T = (1,1,1,1,1,1,1,1,1,1,1,1,1,1,1) \\ 2\mathbf{h}_1^T = (0,-1,-2,-1,0,0,0,0,0,0,1,2,1,0,0) \\ 2\mathbf{h}_2^T = (0,0,0,-1,-2,-1,0,0,0,0,0,0,1,2,1) \\ 4\mathbf{h}_3^T = (0,0,0,1,0,0,0,0,0,0,0,0,1,0,0) \\ 4\mathbf{h}_4^T = (0,0,0,-1,0,0,0,0,0,0,0,0,1,0,0) \\ 4\mathbf{h}_5^T = (0,1,4,1,0,0,0,4,0,0,1,4,1,0,0) \\ 4\mathbf{h}_6^T = (0,0,0,1,4,1,0,0,4,0,0,0,1,4,1) \\ \mathbf{h}_7^T = (1,1,1,1,1,1,0,0,0,1,1,1,1,1,1) \\ 4\mathbf{h}_8^T = (0,-1,-4,-1,0,0,0,0,0,0,1,4,1,0,0) \\ 4\mathbf{h}_9^T = (0,0,0,-1,-4,-1,0,0,0,0,0,0,1,4,1) \\ 2\mathbf{h}_{10}^T = (0,1,2,1,0,0,0,0,0,0,1,2,1,0,0) \\ 2\mathbf{h}_{11}^T = (0,0,0,1,2,1,0,0,0,0,0,0,1,2,1) \end{cases}$$

To determine the unknown constants a_{ji} and $c_{\alpha i}$ in Eq. (2), the derivatives of the shape functions, evaluated at the origin of the reference frame, are introduced:

$$\mathbf{b}_i = \mathbf{N}_{,i}(\mathbf{0}) = \frac{\partial \mathbf{N}}{\partial x_i}_{|\xi=\eta=\zeta=0} \quad i = 1, 2, 3 \tag{4}$$

where vector $\mathbf{N}$ has as components the shape functions N_I. Explicit expressions for vectors $\mathbf{b}_i$ can be derived by algebra, which allow us to demonstrate the following orthogonality conditions:

$$\mathbf{b}_i^T \cdot \mathbf{h}_\alpha = 0, \mathbf{b}_i^T \cdot \mathbf{s} = 0, \mathbf{b}_i^T \cdot \mathbf{x}_j = \delta_{ij},\ i, j = 1, \ldots, 3$$

$$\mathbf{h}_1^T \cdot \mathbf{s} = 0, \mathbf{h}_2^T \cdot \mathbf{s} = 0, 2\mathbf{h}_3^T \cdot \mathbf{s} = 1, \mathbf{h}_4^T \cdot \mathbf{s} = 0, \mathbf{h}_5^T \cdot \mathbf{s} = 4, \mathbf{h}_6^T \cdot \mathbf{s} = 4,$$

$$\mathbf{h}_7^T \cdot \mathbf{s} = 12, \mathbf{h}_8^T \cdot \mathbf{s} = 0, \mathbf{h}_9^T \cdot \mathbf{s} = 0, \mathbf{h}_{10}^T \cdot \mathbf{s} = 4, \mathbf{h}_{11}^T \cdot \mathbf{s} = 4$$

$$8\mathbf{h}_\alpha^T \cdot \mathbf{h}_\beta = \begin{bmatrix} 24 & -4 & 0 & 2 & 0 & 0 & 0 & 20 & 2 & 0 & 0 \\ -4 & 24 & 0 & 2 & 0 & 0 & 0 & 2 & 20 & 0 & 0 \\ 0 & 0 & 1 & 0 & 1 & 1 & 4 & 0 & 0 & 2 & 2 \\ 2 & 2 & 0 & 1 & 0 & 0 & 0 & 1 & 1 & 0 & 0 \\ 0 & 0 & 1 & 0 & 26 & 1 & 24 & 0 & 0 & 20 & 2 \\ 0 & 0 & 1 & 0 & 1 & 26 & 24 & 0 & 0 & 2 & 20 \\ 0 & 0 & 4 & 0 & 24 & 24 & 96 & 0 & 0 & 32 & 32 \\ 20 & 2 & 0 & 1 & 0 & 0 & 0 & 18 & 1 & 0 & 0 \\ 2 & 20 & 0 & 1 & 0 & 0 & 0 & 1 & 18 & 0 & 0 \\ 0 & 0 & 2 & 0 & 20 & 2 & 32 & 0 & 0 & 24 & 4 \\ 0 & 0 & 2 & 0 & 2 & 20 & 32 & 0 & 0 & 4 & 24 \end{bmatrix} \tag{5}$$

The constants a_{ji} and $c_{\alpha i}$ can be then determined by the scalar product of (3) by $\mathbf{b}_j^T$, $\mathbf{s}^T$, and $\mathbf{h}_\alpha^T$, successively, and the use of orthogonality conditions (5):

$$a_{ji} = \mathbf{b}_j^T \cdot \mathbf{d}_i, \quad c_{\alpha i} = \boldsymbol{\gamma}_\alpha^T \cdot \mathbf{d}_i, \tag{6}$$

with

$$\begin{aligned} \boldsymbol{\gamma}_\alpha^T = {} & n_{\alpha 1}\left(\mathbf{h}_1^T - \left(\mathbf{h}_1^T \cdot \mathbf{x}_j\right)\mathbf{b}_j^T\right) + n_{\alpha 2}\left(\mathbf{h}_2^T - \left(\mathbf{h}_2^T \cdot \mathbf{x}_j\right)\mathbf{b}_j^T\right) \\ & + n_{\alpha 3}\left[\left(\mathbf{h}_3^T - \frac{1}{30}\mathbf{s}^T\right) - \left(\left(\mathbf{h}_3^T - \frac{1}{30}\mathbf{s}^T\right) \cdot \mathbf{x}_j\right)\mathbf{b}_j^T\right] \\ & + n_{\alpha 4}\left(\mathbf{h}_4^T - \left(\mathbf{h}_4^T \cdot \mathbf{x}_j\right)\mathbf{b}_j^T\right) \\ & + n_{\alpha 5}\left[\left(\mathbf{h}_5^T - \frac{4}{15}\mathbf{s}^T\right) - \left(\left(\mathbf{h}_5^T - \frac{4}{15}\mathbf{s}^T\right) \cdot \mathbf{x}_j\right)\mathbf{b}_j^T\right] \\ & + n_{\alpha 6}\left(\left(\mathbf{h}_6^T - \frac{4}{15}\mathbf{s}^T\right) - \left(\left(\mathbf{h}_6^T - \frac{4}{15}\mathbf{s}^T\right) \cdot \mathbf{x}_j\right)\mathbf{b}_j^T\right) \\ & + n_{\alpha 7}\left(\left(\mathbf{h}_7^T - \frac{4}{5}\mathbf{s}^T\right) - \left(\left(\mathbf{h}_7^T - \frac{4}{5}\mathbf{s}^T\right) \cdot \mathbf{x}_j\right)\mathbf{b}_j^T\right) \\ & + n_{\alpha 8}\left(\mathbf{h}_8^T - \left(\mathbf{h}_8^T \cdot \mathbf{x}_j\right)\mathbf{b}_j^T\right) + n_{\alpha 9}\left(\mathbf{h}_9^T - \left(\mathbf{h}_9^T \cdot \mathbf{x}_j\right)\mathbf{b}_j^T\right) \\ & + n_{\alpha 10}\left(\left(\mathbf{h}_{10}^T - \frac{4}{15}\mathbf{s}^T\right) - \left(\left(\mathbf{h}_{10}^T - \frac{4}{15}\mathbf{s}^T\right) \cdot \mathbf{x}_j\right)\mathbf{b}_j^T\right) \\ & + n_{\alpha 11}\left(\left(\mathbf{h}_{11}^T - \frac{4}{15}\mathbf{s}^T\right) - \left(\left(\mathbf{h}_{11}^T - \frac{4}{15}\mathbf{s}^T\right) \cdot \mathbf{x}_j\right)\mathbf{b}_j^T\right) \end{aligned}$$

and

$$\left[\mathbf{n}_{\alpha\beta}\right] = \begin{bmatrix} \frac{17}{2} & 0 & 0 & -8 & 0 & 0 & 0 & -9 & 0 & 0 & 0 \\ 0 & \frac{17}{2} & 0 & -8 & 0 & 0 & 0 & 0 & -9 & 0 & 0 \\ 0 & 0 & \frac{256}{17} & 0 & \frac{36}{17} & \frac{36}{17} & 2 & 0 & 0 & -\frac{58}{17} & -\frac{58}{17} \\ -8 & -8 & 0 & 24 & 0 & 0 & 0 & 8 & 8 & 0 & 0 \\ 0 & 0 & \frac{36}{17} & 0 & \frac{316}{187} & \frac{146}{187} & 1 & 0 & 0 & -\frac{324}{187} & -\frac{171}{187} \\ 0 & 0 & \frac{36}{17} & 0 & \frac{146}{187} & \frac{316}{187} & 1 & 0 & 0 & -\frac{171}{187} & -\frac{324}{187} \\ 0 & 0 & 2 & 0 & 1 & 1 & \frac{3}{2} & 0 & 0 & -\frac{3}{2} & -\frac{3}{2} \\ -9 & 0 & 0 & 8 & 0 & 0 & 0 & 10 & 0 & 0 & 0 \\ 0 & -9 & 0 & 8 & 0 & 0 & 0 & 0 & 10 & 0 & 0 \\ 0 & 0 & -\frac{58}{17} & 0 & -\frac{324}{187} & -\frac{171}{187} & -\frac{3}{2} & 0 & 0 & \frac{505}{187} & \frac{585}{374} \\ 0 & 0 & -\frac{58}{17} & 0 & -\frac{171}{187} & -\frac{324}{187} & -\frac{3}{2} & 0 & 0 & \frac{585}{374} & \frac{505}{187} \end{bmatrix}$$

$$\alpha, \beta = 1, 2, \ldots, 11$$

In the case of the SHB20 element, repeating exactly the same steps results in

$$\begin{cases} u_i = a_{0i} + a_{1i}x_1 + a_{2i}x_2 + a_{3i}x_3 + c_{1i}h_1 + c_{2i}h_2 + c_{3i}h_3 + c_{4i}h_4 + c_{5i}h_5 \\ \qquad +c_{6i}h_6 + c_{7i}h_7 + c_{8i}h_8 + c_{9i}h_9 + c_{10i}h_{10} + c_{11i}h_{11} + c_{12i}h_{12} + c_{13i}h_{13} \\ \qquad +c_{14i}h_{14} + c_{15i}h_{15} + c_{16i}h_{16} \\ h_1 = \xi\zeta, h_2 = \eta\zeta, h_3 = \xi\eta, h_4 = \xi^2, h_5 = \eta^2, h_6 = \zeta^2, h_7 = \xi\eta\zeta, h_8 = \xi^2\eta, \\ h_9 = \xi^2\zeta, h_{10} = \eta^2\xi, h_{11} = \eta^2\zeta, h_{12} = \zeta^2\xi, h_{13} = \zeta^2\eta, h_{14} = \xi^2\eta\zeta, h_{15} = \xi\eta^2\zeta, \\ h_{16} = \xi\eta\zeta^2 \end{cases}$$

which, evaluated at the element nodes, yields the three twenty-equation systems:

$$\mathbf{d}_i = a_{0i}\mathbf{s} + a_{1i}\mathbf{x}_1 + a_{2i}\mathbf{x}_2 + a_{3i}\mathbf{x}_3 + c_{1i}\mathbf{h}_1 + c_{2i}\mathbf{h}_2 + c_{3i}\mathbf{h}_3 + \cdots + c_{16i}\mathbf{h}_{16},$$
$$i = 1, 2, 3. \tag{7}$$

As before, the twenty-component vectors $\mathbf{d}_i$ and $\mathbf{x}_i$ indicate here the nodal displacements and coordinates, while $\mathbf{s}$ and $\mathbf{h}_\alpha (\alpha = 1, \ldots, 16)$ are given by

$$
\begin{cases}
\mathbf{s}^T = (1,1,1,1,1,1,1,1,1,1,1,1,1,1,1,1,1,1,1,1) \\
\mathbf{h}_1^T = (1,-1,-1,1,-1,1,1,-1,0,-1,0,1,0,0,0,0,0,1,0,-1) \\
\mathbf{h}_2^T = (1,1,-1,-1,-1,-1,1,1,1,0,-1,0,0,0,0,0,-1,0,1,0) \\
\mathbf{h}_3^T = (1,-1,1,-1,1,-1,1,-1,0,0,0,0,1,-1,1,-1,0,0,0,0) \\
\mathbf{h}_4^T = (1,1,1,1,1,1,1,1,0,1,0,1,1,1,1,1,0,1,0,1) \\
\mathbf{h}_5^T = (1,1,1,1,1,1,1,1,1,0,1,0,1,1,1,1,1,0,1,0) \\
\mathbf{h}_6^T = (1,1,1,1,1,1,1,1,1,1,1,1,0,0,0,0,1,1,1,1) \\
\mathbf{h}_7^T = (-1,1,-1,1,1,-1,1,-1,0,0,0,0,0,0,0,0,0,0,0,0) \\
\mathbf{h}_8^T = (-1,-1,1,1,-1,-1,1,1,0,0,0,0,-1,-1,1,1,0,0,0,0) \\
\mathbf{h}_9^T = (-1,-1,-1,-1,1,1,1,1,0,-1,0,-1,0,0,0,0,0,1,0,1) \\
\mathbf{h}_{10}^T = (-1,1,1,-1,-1,1,1,-1,0,0,0,0,-1,1,1,-1,0,0,0,0) \\
\mathbf{h}_{11}^T = (-1,-1,-1,-1,1,1,1,1,-1,0,-1,0,0,0,0,0,1,0,1,0) \\
\mathbf{h}_{12}^T = (-1,1,1,-1,-1,1,1,-1,0,1,0,-1,0,0,0,0,0,1,0,-1) \\
\mathbf{h}_{13}^T = (-1,-1,1,1,-1,-1,1,1,-1,0,1,0,0,0,0,0,-1,0,1,0) \\
\mathbf{h}_{14}^T = (1,1,-1,-1,-1,-1,1,1,0,0,0,0,0,0,0,0,0,0,0,0) \\
\mathbf{h}_{15}^T = (1,-1,-1,1,-1,1,1,-1,0,0,0,0,0,0,0,0,0,0,0,0) \\
\mathbf{h}_{16}^T = (1,-1,1,-1,1,-1,1,-1,0,0,0,0,0,0,0,0,0,0,0,0)
\end{cases}
$$

In the same way, the introduction of the twenty-component vectors $\mathbf{b}_i$, defined by Eq. (4), allows us to demonstrate the following orthogonality conditions:

$$
\mathbf{b}_i^T \cdot \mathbf{h}_\alpha = 0, \mathbf{b}_i^T \cdot \mathbf{s} = 0, \mathbf{b}_i^T \cdot \mathbf{x}_j = \delta_{ij}, i, j = 1, \ldots, 3
$$

$$
\mathbf{h}_1^T \cdot \mathbf{s} = 0, \mathbf{h}_2^T \cdot \mathbf{s} = 0, \mathbf{h}_3^T \cdot \mathbf{s} = 0, \mathbf{h}_4^T \cdot \mathbf{s} = 16, \mathbf{h}_5^T \cdot \mathbf{s} = 16,
$$

$$
\mathbf{h}_6^T \cdot \mathbf{s} = 16, \mathbf{h}_7^T \cdot \mathbf{s} = 0, \mathbf{h}_8^T \cdot \mathbf{s} = 0, \mathbf{h}_9^T \cdot \mathbf{s} = 0, \mathbf{h}_{10}^T \cdot \mathbf{s} = 0,
$$

$$
\mathbf{h}_{11}^T \cdot \mathbf{s} = 0, \mathbf{h}_{12}^T \cdot \mathbf{s} = 0, \mathbf{h}_{13}^T \cdot \mathbf{s} = 0, \mathbf{h}_{14}^T \cdot \mathbf{s} = 0, \mathbf{h}_{15}^T \cdot \mathbf{s} = 0, \mathbf{h}_{16}^T \cdot \mathbf{s} = 0
$$

$$
\mathbf{h}_\alpha^T \cdot \mathbf{h}_\beta = \begin{bmatrix}
12 & 0 & 0 & 0 & 0 & 0 & 0 & 0 & 0 & 0 & 0 & 0 & 0 & 0 & 8 & 0 \\
0 & 12 & 0 & 0 & 0 & 0 & 0 & 0 & 0 & 0 & 0 & 0 & 0 & 8 & 0 & 0 \\
0 & 0 & 12 & 0 & 0 & 0 & 0 & 0 & 0 & 0 & 0 & 0 & 0 & 0 & 0 & 8 \\
0 & 0 & 0 & 16 & 12 & 12 & 0 & 0 & 0 & 0 & 0 & 0 & 0 & 0 & 0 & 0 \\
0 & 0 & 0 & 12 & 16 & 12 & 0 & 0 & 0 & 0 & 0 & 0 & 0 & 0 & 0 & 0 \\
0 & 0 & 0 & 12 & 12 & 16 & 0 & 0 & 0 & 0 & 0 & 0 & 0 & 0 & 0 & 0 \\
0 & 0 & 0 & 0 & 0 & 0 & 8 & 0 & 0 & 0 & 0 & 0 & 0 & 0 & 0 & 0 \\
0 & 0 & 0 & 0 & 0 & 0 & 0 & 12 & 0 & 0 & 0 & 0 & 8 & 0 & 0 & 0 \\
0 & 0 & 0 & 0 & 0 & 0 & 0 & 0 & 12 & 0 & 8 & 0 & 0 & 0 & 0 & 0 \\
0 & 0 & 0 & 0 & 0 & 0 & 0 & 0 & 0 & 12 & 0 & 8 & 0 & 0 & 0 & 0 \\
0 & 0 & 0 & 0 & 0 & 0 & 0 & 0 & 8 & 0 & 12 & 0 & 0 & 0 & 0 & 0 \\
0 & 0 & 0 & 0 & 0 & 0 & 0 & 0 & 0 & 8 & 0 & 12 & 0 & 0 & 0 & 0 \\
0 & 0 & 0 & 0 & 0 & 0 & 0 & 8 & 0 & 0 & 0 & 0 & 12 & 0 & 0 & 0 \\
0 & 8 & 0 & 0 & 0 & 0 & 0 & 0 & 0 & 0 & 0 & 0 & 0 & 8 & 0 & 0 \\
8 & 0 & 0 & 0 & 0 & 0 & 0 & 0 & 0 & 0 & 0 & 0 & 0 & 0 & 8 & 0 \\
0 & 0 & 8 & 0 & 0 & 0 & 0 & 0 & 0 & 0 & 0 & 0 & 0 & 0 & 0 & 8
\end{bmatrix}
$$

Using the above conditions along with the successive scalar product of (7) by $\mathbf{b}_j^T$, $\mathbf{s}^T$, and $\mathbf{h}_\alpha^T$ leads to the same expression (6) for the constants a_{ji} and $c_{\alpha i}$; however, the corresponding vectors $\boldsymbol{\gamma}_\alpha$ must be replaced now by

$$
\begin{aligned}
\boldsymbol{\gamma}_\alpha^T = {} & n_{\alpha 1}\left(\mathbf{h}_1^T - \left(\mathbf{h}_1^T \cdot \mathbf{x}_j\right)\mathbf{b}_j^T\right) + n_{\alpha 2}\left(\mathbf{h}_2^T - \left(\mathbf{h}_2^T \cdot \mathbf{x}_j\right)\mathbf{b}_j^T\right) \\
& + n_{\alpha 3}\left(\mathbf{h}_3^T - \left(\mathbf{h}_3^T \cdot \mathbf{x}_j\right)\mathbf{b}_j^T\right) + n_{\alpha 4}\left[\left(\mathbf{h}_4^T - \frac{4}{5}\mathbf{s}^T\right) - \left(\left(\mathbf{h}_4^T - \frac{4}{5}\mathbf{s}^T\right)\cdot \mathbf{x}_j\right)\mathbf{b}_j^T\right] \\
& + n_{\alpha 5}\left[\left(\mathbf{h}_5^T - \frac{4}{5}\mathbf{s}^T\right) - \left(\left(\mathbf{h}_5^T - \frac{4}{5}\mathbf{s}^T\right)\cdot \mathbf{x}_j\right)\mathbf{b}_j^T\right] \\
& + n_{\alpha 6}\left[\left(\mathbf{h}_6^T - \frac{4}{5}\mathbf{s}^T\right) - \left(\left(\mathbf{h}_6^T - \frac{4}{5}\mathbf{s}^T\right)\cdot \mathbf{x}_j\right)\mathbf{b}_j^T\right] \\
& + n_{\alpha 7}\left(\mathbf{h}_7^T - \left(\mathbf{h}_7^T \cdot \mathbf{x}_j\right)\mathbf{b}_j^T\right) + n_{\alpha 8}\left(\mathbf{h}_8^T - \left(\mathbf{h}_8^T \cdot \mathbf{x}_j\right)\mathbf{b}_j^T\right) \\
& + n_{\alpha 9}\left(\mathbf{h}_9^T - \left(\mathbf{h}_9^T \cdot \mathbf{x}_j\right)\mathbf{b}_j^T\right) + n_{\alpha 10}\left(\mathbf{h}_{10}^T - \left(\mathbf{h}_{10}^T \cdot \mathbf{x}_j\right)\mathbf{b}_j^T\right) \\
& + n_{\alpha 11}\left(\mathbf{h}_{11}^T - \left(\mathbf{h}_{11}^T \cdot \mathbf{x}_j\right)\mathbf{b}_j^T\right) + n_{\alpha 12}\left(\mathbf{h}_{12}^T - \left(\mathbf{h}_{12}^T \cdot \mathbf{x}_j\right)\mathbf{b}_j^T\right) \\
& + n_{\alpha 13}\left(\mathbf{h}_{13}^T - \left(\mathbf{h}_{13}^T \cdot \mathbf{x}_j\right)\mathbf{b}_j^T\right) + n_{\alpha 14}\left(\mathbf{h}_{14}^T - \left(\mathbf{h}_{14}^T \cdot \mathbf{x}_j\right)\mathbf{b}_j^T\right) \\
& + n_{\alpha 15}\left(\mathbf{h}_{15}^T - \left(\mathbf{h}_{15}^T \cdot \mathbf{x}_j\right)\mathbf{b}_j^T\right) + n_{\alpha 16}\left(\mathbf{h}_{16}^T - \left(\mathbf{h}_{16}^T \cdot \mathbf{x}_j\right)\mathbf{b}_j^T\right)
\end{aligned}
$$

with

$$
\left[\mathbf{n}_{\alpha\beta}\right] = \begin{bmatrix}
\frac{1}{4} & 0 & 0 & 0 & 0 & 0 & 0 & 0 & 0 & 0 & 0 & 0 & 0 & -\frac{1}{4} & 0 \\
0 & \frac{1}{4} & 0 & 0 & 0 & 0 & 0 & 0 & 0 & 0 & 0 & 0 & -\frac{1}{4} & 0 & 0 \\
0 & 0 & \frac{1}{4} & 0 & 0 & 0 & 0 & 0 & 0 & 0 & 0 & 0 & 0 & 0 & -\frac{1}{4} \\
0 & 0 & 0 & \frac{3}{8} & \frac{1}{8} & \frac{1}{8} & 0 & 0 & 0 & 0 & 0 & 0 & 0 & 0 & 0 \\
0 & 0 & 0 & \frac{1}{8} & \frac{3}{8} & \frac{1}{8} & 0 & 0 & 0 & 0 & 0 & 0 & 0 & 0 & 0 \\
0 & 0 & 0 & \frac{1}{8} & \frac{1}{8} & \frac{3}{8} & 0 & 0 & 0 & 0 & 0 & 0 & 0 & 0 & 0 \\
0 & 0 & 0 & 0 & 0 & 0 & \frac{1}{8} & 0 & 0 & 0 & 0 & 0 & 0 & 0 & 0 \\
0 & 0 & 0 & 0 & 0 & 0 & 0 & \frac{3}{20} & 0 & 0 & 0 & -\frac{1}{10} & 0 & 0 & 0 \\
0 & 0 & 0 & 0 & 0 & 0 & 0 & 0 & \frac{3}{20} & 0 & -\frac{1}{10} & 0 & 0 & 0 & 0 \\
0 & 0 & 0 & 0 & 0 & 0 & 0 & 0 & 0 & \frac{3}{20} & 0 & -\frac{1}{10} & 0 & 0 & 0 \\
0 & 0 & 0 & 0 & 0 & 0 & 0 & 0 & -\frac{1}{10} & 0 & \frac{3}{20} & 0 & 0 & 0 & 0 \\
0 & 0 & 0 & 0 & 0 & 0 & 0 & 0 & 0 & -\frac{1}{10} & 0 & \frac{3}{20} & 0 & 0 & 0 \\
0 & 0 & 0 & 0 & 0 & 0 & 0 & -\frac{1}{10} & 0 & 0 & 0 & 0 & \frac{3}{20} & 0 & 0 \\
0 & -\frac{1}{4} & 0 & 0 & 0 & 0 & 0 & 0 & 0 & 0 & 0 & 0 & 0 & \frac{1}{8} & 0 \\
-\frac{1}{4} & 0 & 0 & 0 & 0 & 0 & 0 & 0 & 0 & 0 & 0 & 0 & 0 & 0 & \frac{1}{8} \\
0 & 0 & -\frac{1}{4} & 0 & 0 & 0 & 0 & 0 & 0 & 0 & 0 & 0 & 0 & 0 & 0
\end{bmatrix}
$$

$\alpha, \beta = 1, 2, \ldots, 16$

After these lengthy derivations, the following expressions for the displacement gradient $u_{i,j}$ and for the discrete gradient operator $\mathbf{B}$, which relates the strain field to the nodal displacements by the relationship $\nabla_s(\mathbf{u}) = \mathbf{B} \cdot \mathbf{d}$, are found:

$$u_{i,j} = \left(\mathbf{b}_j^T + h_{\alpha,j}\boldsymbol{\gamma}_\alpha^T\right) \cdot \mathbf{d}_i, \tag{8}$$

$$\mathbf{B} = \begin{bmatrix} \mathbf{b}_x^T + h_{\alpha,x}\boldsymbol{\gamma}_\alpha^T & \mathbf{0} & \mathbf{0} \\ \mathbf{0} & \mathbf{b}_y^T + h_{\alpha,y}\boldsymbol{\gamma}_\alpha^T & \mathbf{0} \\ \mathbf{0} & \mathbf{0} & \mathbf{b}_z^T + h_{\alpha,z}\boldsymbol{\gamma}_\alpha^T \\ \mathbf{b}_y^T + h_{\alpha,y}\boldsymbol{\gamma}_\alpha^T & \mathbf{b}_x^T + h_{\alpha,x}\boldsymbol{\gamma}_\alpha^T & \mathbf{0} \\ \mathbf{0} & \mathbf{b}_z^T + h_{\alpha,z}\boldsymbol{\gamma}_\alpha^T & \mathbf{b}_y^T + h_{\alpha,y}\boldsymbol{\gamma}_\alpha^T \\ \mathbf{b}_z^T + h_{\alpha,z}\boldsymbol{\gamma}_\alpha^T & \mathbf{0} & \mathbf{b}_x^T + h_{\alpha,x}\boldsymbol{\gamma}_\alpha^T \end{bmatrix}, \tag{9}$$

with

$$\nabla_s(\mathbf{u}) = \begin{bmatrix} u_{x,x} \\ u_{y,y} \\ u_{z,z} \\ u_{x,y} + u_{y,x} \\ u_{y,z} + u_{z,y} \\ u_{x,z} + u_{z,x} \end{bmatrix}, \qquad \mathbf{d} = \begin{bmatrix} \mathbf{d}_x \\ \mathbf{d}_y \\ \mathbf{d}_z \end{bmatrix}.$$

Note that Eqs. (8) and (9) are common to both elements, provided that the summation over subscript α is taken from 1 to 11 for the SHB15, and from 1 to 16 for the SHB20. The compact expression (9) for the discrete gradient operator $\mathbf{B}$ is very convenient because the $\boldsymbol{\gamma}_\alpha$ vectors involved are shown to satisfy the following orthogonality conditions:

$$\boldsymbol{\gamma}_\alpha^T \cdot \mathbf{x}_j = 0,\ \boldsymbol{\gamma}_\alpha^T \cdot \mathbf{h}_\beta = \delta_{\alpha\beta},\ j = 1, \ldots, 3,\ (\alpha, \beta = 1, \ldots, 11) \text{ resp. } (\alpha, \beta = 1, \ldots, 16).$$

This would allow each of the deformation modes to be separately handled in order to build a simple form for an assumed-strain field. The formulation (9) also allows us to check any stiffness matrix rank deficiency for these elements. It is noteworthy that no projection for the corresponding discrete gradient operators has been applied to these quadratic solid–shell elements, as no significant locking has been experienced so far in the benchmark problems tested.

2.3 Variational principle

The Hu–Washizu mixed variational principle, which was used for the formulation of the linear solid–shell elements SHB8PS and SHB6 [31,32], is considered here again. More specifically, a simplified form of this principle, as described by Simo and Hughes [34], is adopted, which can be written for a single finite element as

$$\pi(\dot{\bar{\boldsymbol{\varepsilon}}}) = \int_{\Omega_e} \delta\dot{\bar{\boldsymbol{\varepsilon}}}^T \cdot \boldsymbol{\sigma}\, d\Omega - \delta\dot{\mathbf{d}}^T \cdot \mathbf{f}^{ext} = 0, \tag{10}$$

where δ denotes a variation, $\dot{\bar{\boldsymbol{\varepsilon}}}$ the assumed-strain rate, $\boldsymbol{\sigma}$ the stress field evaluated from the constitutive equations, $\dot{\mathbf{d}}$ the nodal velocities, and $\mathbf{f}^{ext}$ the external nodal forces. The well-known assumed-strain method consists of choosing a $\bar{\mathbf{B}}$ operator, obtained by projection of the classical discrete gradient operator $\mathbf{B}$, such as $\dot{\bar{\boldsymbol{\varepsilon}}} = \bar{\mathbf{B}} \cdot \dot{\mathbf{d}}$. The goal of this method is to eliminate most of the locking phenomena (e.g., shear locking, membrane locking, etc) that can be encountered, especially in low-order finite elements. Although this technique has been shown to be consistent, from a variational perspective, with the Hu–Washizu variational principle [34], this variational justification does not provide a general, systematic way to derive adequate assumed-strain fields.

Substituting the stress tensor $\boldsymbol{\sigma}$ in Eq. (10) with the Hooke law $\boldsymbol{\sigma} = \mathbf{C} \cdot \bar{\boldsymbol{\varepsilon}}$, where $\mathbf{C}$ is the elasticity matrix, and using the relationship $\dot{\bar{\boldsymbol{\varepsilon}}} = \bar{\mathbf{B}} \cdot \dot{\mathbf{d}}$ yields

$$\mathbf{K}_e = \int_{\Omega_e} \bar{\mathbf{B}}^T \cdot \mathbf{C} \cdot \bar{\mathbf{B}} d\Omega, \quad \mathbf{f}^{int} = \int_{\Omega_e} \bar{\mathbf{B}}^T \cdot \boldsymbol{\sigma}(\dot{\bar{\boldsymbol{\varepsilon}}})\, d\Omega, \tag{11}$$

where $\mathbf{K}_e$ and $\mathbf{f}^{int}$ denote the stiffness matrix and the internal force vector, respectively.

For the above-mentioned reasons related to the absence of locking for the proposed quadratic solid–shell elements in the benchmark problems tested, no projection for the corresponding discrete gradient operators has been applied here. This amounts to taking $\bar{\mathbf{B}} = \mathbf{B}$ in Eq. (11), which leads to the following classical expressions for the stiffness matrix and internal forces:

$$\mathbf{K}_e = \int_{\Omega_e} \mathbf{B}^T \cdot \mathbf{C} \cdot \mathbf{B} d\Omega = \sum_{I_n=1}^{N_{\text{int}}} \omega(\zeta_{I_n}) J(\zeta_{I_n}) \mathbf{B}^T(\zeta_{I_n}) \cdot \mathbf{C} \cdot \mathbf{B}_(\zeta_{I_n}),$$

and

$$\mathbf{f}^{int} = \int_{\Omega_e} \mathbf{B}^T \cdot \boldsymbol{\sigma}\, d\Omega = \sum_{I_n=1}^{N_{\text{int}}} \omega(\zeta_{I_n}) J(\zeta_{I_n}) \mathbf{B}^T(\zeta_{I_n}) \cdot \boldsymbol{\sigma}(\zeta_{I_n}).$$

In the above equations, which are common to both developed elements, $J(\zeta_{I_n})$ is the Jacobian of the transformation between the reference configuration and the current configuration of the element, $\omega(\zeta_{I_n})$ is the weight associated with the Gauss point I_n, and the total number of integration points N_{int} is to adapt depending on the element considered: $N_{\text{int}} = 3 \times n_{\text{int}}$ for the SHB15, and $N_{\text{int}} = 4 \times n_{\text{int}}$ for the SHB20.

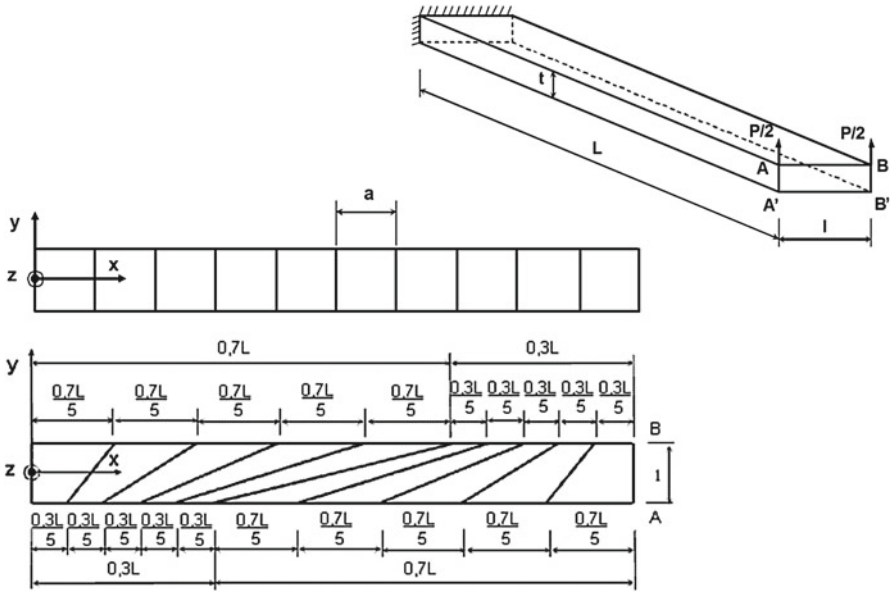

Fig. 2 Test of admissible aspect ratios: Cantilever beam geometry and mesh description

3 Numerical tests and performance evaluation

In this section, the performance of the proposed solid–shell elements will be assessed based on the analysis of a set of selective and representative linear benchmark problems. Recall that the formulation of the SHB15 and SHB20 is valid for any number of through-thickness integration points n_{int}, with a minimum number of two. This user-defined number n_{int} is taken equal to two in linear elastic problems, but can be freely modified whenever required for a specific application. To illustrate the performance of the proposed elements, the results obtained for each test problem will be compared to the reference solution and also to the results yielded by other existing finite elements having similar properties in terms of geometry, number of nodes and degrees of freedom.

3.1 Test of the maximum aspect ratios

This linear test is specifically designed to evaluate the aspect ratio limits of the elements on a beam bending problem. It was previously applied to the linear solid–shell SHB8PS [35] in order to assess the behavior of the element when non-structured, irregular meshes are employed and to analyze potential locking phenomena in the limit of high aspect ratios. The corresponding cantilever beam geometry is shown in Fig. 2, where regular and irregular mesh data are specified.

In this analysis, the length and the width of the beam are fixed: $\mathrm{L} = 100, \mathrm{l} = 10$; while the thickness t is a varying parameter. The elastic properties are $E = 68.25 \times 10^6$

Table 1 Normalized displacement at point A for the regular mesh

Aspect ratio (r = l/t)	HEX20	SHB20	PRI15	SHB15
	u_z/u_z^{ref}	u_z/u_z^{ref}	u_z/u_z^{ref}	u_z/u_z^{ref}
1	1.005	1.009	1.000	1.009
10	0.984	0.998	0.975	0.997
100	0.951	0.997	0.967	0.995
200	0.959	0.996	0.953	1.019
333		0.998	0.860	0.988
500		1.004		

Table 2 Normalized displacement at point A for the irregular mesh

Aspect ratio (r = l/t)	HEX20	SHB20	PRI15	SHB15
	u_z/u_z^{ref}	u_z/u_z^{ref}	u_z/u_z^{ref}	u_z/u_z^{ref}
1	0.981	1.010	0.974	0.985
10	0.682	0.997	0.871	0.945
100	0.345	0.995	0.832	0.944
200	0.294	1.002	0.832	0.944
333	0.251	0.984	0.878	0.926

and $\nu = 0.3$. A bending load, P = 4, is applied to the free end of the beam, and the results are normalized using the reference solution, which is here analytical, given by beam theory.

For the hexahedral elements, a fixed mesh of 10 elements with a single element along the thickness is used in both regular and irregular meshes. For the regular mesh, each element is a 10×10 square (i.e., $l = 10$ is the side of the square, and r = l/t represents the varying aspect ratio). A similar aspect-ratio definition is adopted for the irregular mesh (see Fig. 2). For the prismatic elements, the same procedure as before is followed; then each hexahedron is divided into two prismatic elements, while maintaining a single element layer along the thickness. The normalized vertical displacement at point *A* for different aspect ratios is reported in Table 1, for the regular mesh, and in Table 2 for the irregular mesh.

In Tables 1 and 2, the proposed solid–shells are compared to their conventional 3D counterparts denoted as PRI15 and HEX20. The latter designate the standard full-integration solid elements with fifteen and twenty nodes, respectively. We can observe that the proposed solid–shells perform much better than their 3D counterparts, especially for the irregular meshes. In this test and for the regular mesh, the admissible aspect ratio is about 500 for the SHB20 and 333 for the SHB15. By contrast, the quality of the results for the standard solid elements starts declining for much lower aspect ratios, and this is more remarkable for distorted meshes (see Table 2).

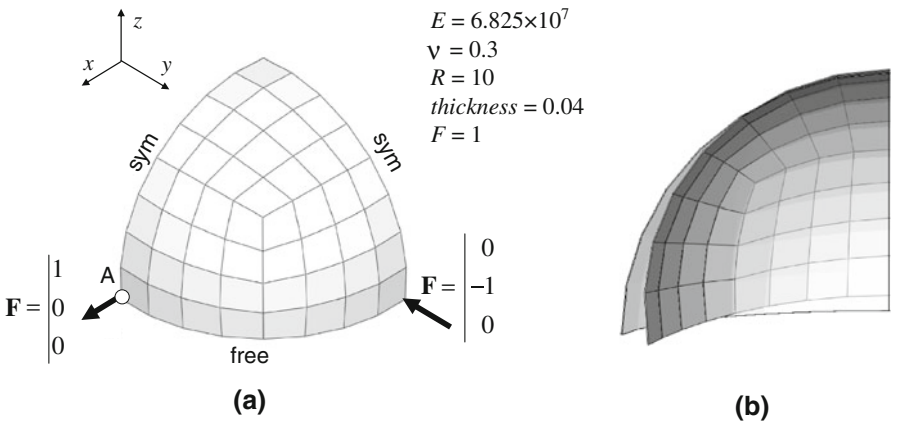

Fig. 3 Test of the pinched hemispherical shell: **a** example of a $3 \times (4 \times 4 \times 1)$ mesh, and **b** initial and deformed configurations

3.2 Test of the pinched hemispherical shell

This doubly-curved shell problem, which is often used to assess the three-dimensional inextensional bending behavior of shells, has become very popular and has been adopted by many authors since it was proposed by MacNeal and Harder [36]. This test is known to be severe because the transverse shear and membrane locking phenomena are dominant and are further accentuated by the particular geometry of the problem (distorted, skewed elements). Figure 3 shows the geometry, loading, and boundary conditions for this elastic thin shell problem ($R/t = 250$). The radius is $R = 10$, the thickness is $t = 0.04$, Young's modulus is $E = 68.25 \times 10^6$, and the Poisson ratio is $\nu = 0.3$.

Owing to the symmetry of the test (i.e., planes (xz) and (yz)), only one quarter of the hemisphere is meshed using a single layer of elements through the thickness and with two unit loads along the directions Ox and Oy. According to the reference solution (MacNeal and Harder [36]), the displacement of point A along the x-direction is $u_x^{ref} = 0.0924$ (see Fig. 3).

The convergence results are reported in Tables 3 and 4 in terms of normalized displacements at point A in the x-direction versus the number of elements. For the hexahedral elements, the mesh nomenclature consists of a $3 \times (N \times N \times 1)$ mesh, in which the quarter of the hemisphere is divided into three zones containing $(N \times N \times 1)$ elements each (see Fig. 3 for an example of a $3 \times (4 \times 4 \times 1)$ mesh). For the prismatic elements, by dividing each hexahedron into two prismatic elements, while maintaining a single element layer through the thickness, the mesh nomenclature becomes $(3 \times (N \times N \times 1)) \times 2$.

The results in Table 3 reveal that the triangular-based elements, SHB15 and PRI15, have a similar convergence in this test problem. Table 4 shows, however, that the quadrangular-based elements converge more rapidly, with a markedly improved performance for the SHB20 as compared to the HEX20.

Table 3 Normalized displacement at point A of pinched hemispherical shell (prismatic elements)

Mesh	PRI15	SHB15
	u_x/u_x^{ref}	u_x/u_x^{ref}
$(3 \times (5 \times 5 \times 1)) \times 2$	0.229	0.168
$(3 \times (10 \times 10 \times 1)) \times 2$	0.795	0.708
$(3 \times (15 \times 15 \times 1)) \times 2$	0.954	0.934
$(3 \times (20 \times 20 \times 1)) \times 2$	0.981	0.974
$(3 \times (25 \times 25 \times 1)) \times 2$	0.993	0.992

Table 4 Normalized displacement at point A of pinched hemispherical shell (hexahedral elements)

Mesh	HEX20	SHB20
	u_x/u_x^{ref}	u_x/u_x^{ref}
$3 \times (1 \times 1 \times 1)$	0.001	0.115
$3 \times (2 \times 2 \times 1)$	0.014	0.564
$3 \times (3 \times 3 \times 1)$	0.065	0.927
$3 \times (4 \times 4 \times 1)$	0.177	0.985
$3 \times (5 \times 5 \times 1)$	0.342	0.997

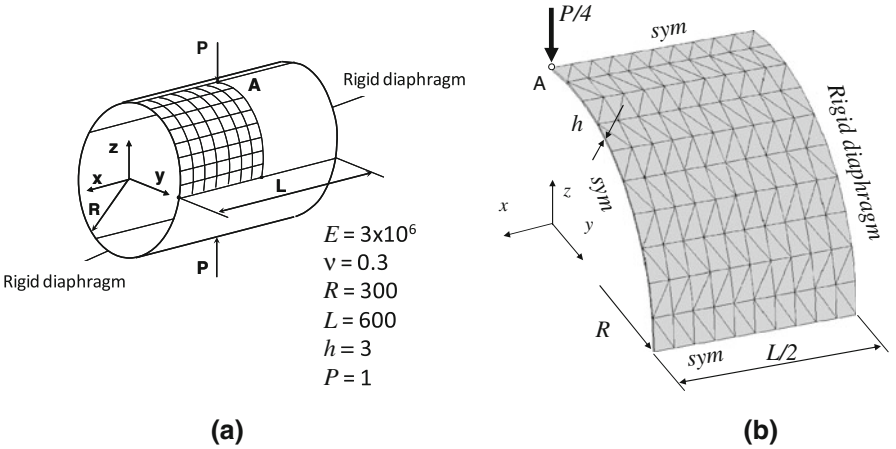

Fig. 4 Test of the pinched cylinder with diaphragms: **a** geometry and data specifications, and **b** example of a $(10 \times 10 \times 1) \times 2$ mesh with prismatic elements

3.3 Test of the pinched cylindrical shell with end diaphragms

A cylindrical shell loaded with a pair of concentrated vertical forces on its middle section is considered here. Both ends of the cylinder are covered with rigid diaphragms that allow displacements only in the axial direction (see Fig. 4). This test has been treated by many authors, among them Belytschko et al. [37] and Chen and Wu [23]. It is considered as a selective test problem since they have shown that shear locking is more severe than membrane locking. The geometric and material parameters for this problem are described in Fig. 4.

Table 5 Normalized displacement at point A of the pinched cylinder (prismatic elements)

Mesh	PRI15	SHB15
	u_z/u_z^{ref}	u_z/u_z^{ref}
$(10 \times 10 \times 1) \times 2$	0.625	0.646
$(15 \times 15 \times 1) \times 2$	0.838	0.913
$(20 \times 20 \times 1) \times 2$	0.919	0.951
$(25 \times 25 \times 1) \times 2$	0.956	0.996

Table 6 Normalized displacement at point A of the pinched cylinder (hexahedral elements)

Mesh	HEX20	SHB20
	u_z/u_z^{ref}	u_z/u_z^{ref}
$4 \times 4 \times 1$	0.140	0.883
$6 \times 6 \times 1$	0.328	0.961
$8 \times 8 \times 1$	0.523	0.979
$10 \times 10 \times 1$	0.675	0.990

Owing to the symmetry of the problem, only one eighth of the cylinder is modeled using different $N \times N \times 1$ meshes for the hexahedral elements, and $(N \times N \times 1) \times 2$ meshes for the prismatic elements. For illustration, an example of a $(10 \times 10 \times 1) \times 2$ mesh is shown in Fig. 4.

The displacement at the load point A in the loading direction is normalized with respect to the reference solution $u_z^{ref} = -0.18248 \times 10^{-4}$, and reported in Tables 5 and 6 for each mesh discretization.

The results in Table 5 reveal once again a similar convergence for the prismatic elements SHB15 and PRI15, with slightly better performance for the SHB15. For the hexahedral elements, Table 6 shows, on the one hand, that their performance is much better than that of the prismatic elements, and on the other hand, that the SHB20 displays a convergence rate significantly better than that of the HEX20.

3.4 Test of buckling of a cylinder under external pressure

This test represents a linear stability analysis of a thin cylinder, which is free at its ends and subjected to a uniformly distributed external pressure. This problem also allows us to verify the formulation of the geometric stiffness matrix $\mathbf{K}_\sigma$. Indeed, in this linear buckling analysis, the Euler critical pressure is determined along with the corresponding buckling mode. This critical state is associated with the lowest pressure that makes the global stiffness matrix singular and is classically obtained by solving the following eigenvalue problem:

$$(\mathbf{K}_e + \lambda_c \mathbf{K}_\sigma) \cdot \mathbf{X}_c = \mathbf{0} \tag{12}$$

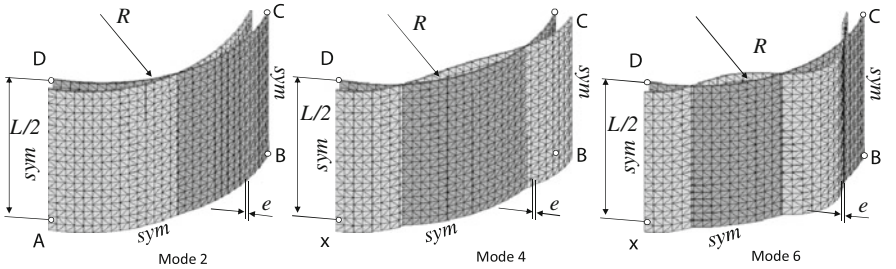

Fig. 5 Buckling of a cylinder under external pressure: buckling modes n^{o} 2, 4, and 6, and example of a $(20 \times 30 \times 1) \times 2$ mesh with prismatic elements

Table 7 Normalized critical pressure for the thin cylinder under pressure (prismatic elements)

Mesh	Mode 2 $P_{cr}^{(2)}/P_{cr(ref)}^{(2)}$		Mode 4 $P_{cr}^{(4)}/P_{cr(ref)}^{(4)}$		Mode 6 $P_{cr}^{(6)}/P_{cr(ref)}^{(6)}$	
	PRI15	SHB15	PRI15	SHB15	PRI15	SHB15
$(10 \times 10 \times 1) \times 2$	1.31	1.43	1.35	1.45	1.42	1.50
$(12 \times 10 \times 1) \times 2$	1.14	1.17	1.16	1.18	1.20	1.20
$(14 \times 10 \times 1) \times 2$	1.07	1.08	1.08	1.08	1.11	1.09
$(16 \times 10 \times 1) \times 2$	1.03	1.03	1.04	1.04	1.06	1.04
$(20 \times 10 \times 1) \times 2$	1.00	1.00	1.01	1.00	1.02	1.00

in which λ_c is the critical buckling load and $\mathbf{X}_c$ is the associated buckling mode. The geometric and material parameters for this test are (see, e.g., Fig. 5): the length $L = 2$, the radius $R = 2$, the thickness $e = 0.02$, Young's modulus $E = 2 \times 10^{11}$, and the Poisson ratio $\nu = 0.3$.

The reference solutions used for comparison are analytical, given by Timoshenko and Gere [38] and Brush and Almroth [39]. Owing to the symmetry, only one eighth of the cylinder is modeled, and symmetry boundary conditions are applied, which in turn restrict the analysis to symmetric buckling modes (i.e., modes 2, 4, and 6 as shown in Fig. 5). The corresponding critical pressure P_{cr} is given by the following analytical expression:

$$P_{cr} = \frac{En^2}{12\left(1-\nu^2\right)}\left(\frac{e}{R}\right)^3, \quad n = 2, 4, 6.$$

The results obtained for the three modes ($n = 2$, 4, and 6) are reported in Tables 7 and 8 in terms of critical pressure, normalized with respect to the analytical reference solution.

Similar to the previous discussion, Table 7 reveals that the SHB15 exhibits a convergence rate comparable to that of the PRI15 on this test problem. On the contrary, Table 8 shows that the SHB20 has remarkable coarse-mesh accuracy and performs much better than its standard solid counterpart HEX20.

Table 8 Normalized critical pressure for the thin cylinder under pressure (hexahedral elements)

Mesh	Mode 2 $P_{cr}^{(2)}/P_{cr(ref)}^{(2)}$		Mode 4 $P_{cr}^{(4)}/P_{cr(ref)}^{(4)}$		Mode 6 $P_{cr}^{(6)}/P_{cr(ref)}^{(6)}$	
	HEX20	SHB20	HEX20	SHB20	HEX20	SHB20
$3 \times 3 \times 1$	53.33	1.00	70.58	1.05	51.73	1.26
$4 \times 4 \times 1$	17.27	0.99	21.14	1.01	25.92	1.07
$5 \times 5 \times 1$	7.60	0.99	8.76	0.99	10.48	1.02
$6 \times 6 \times 1$	4.16	0.98	4.61	0.99	5.31	1.00
$7 \times 7 \times 1$	2.70	0.98	2.91	0.99	3.24	0.99

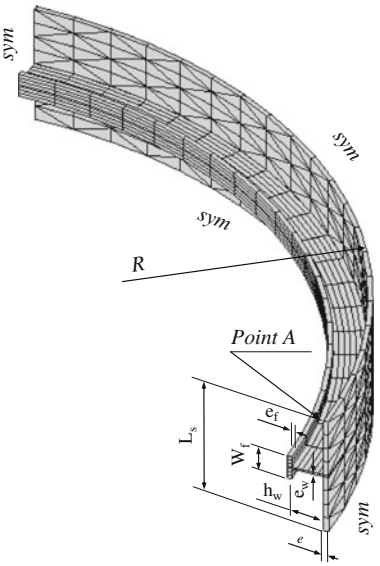

Fig. 6 Geometry and boundary conditions for a quarter of a single ring: an example of a mixed mesh using 260 hexahedral elements for the stiffener and 360 prismatic elements for the main shell

3.5 Test of buckling of a stiffened cylindrical ring

This last benchmark problem also deals with linear elastic stability. The corresponding buckling analysis is based on the eigenvalue equation (12), which allows the formulation of the geometric stiffness matrix $\mathbf{K}_\sigma$ to be checked once again. The test consists of a portion of a submarine hull subjected to external pressure, as illustrated in Fig. 6.

This test was previously used in [40], while in [41] the submarine was modeled in its entirety. The current analysis only considers a single ring, as described in Fig. 6, and the geometric and material data are reported in Table 9.

Note that due to its symmetry, only one quarter of the ring is modeled and subjected to the corresponding symmetry boundary conditions (see Fig. 6). A linear buckling analysis is performed to determine the Euler critical pressure, based on the eigenvalue analysis of the global stiffness matrix (see Eq. (12)). The SHB8PS element is first used to determine a reference solution for the first critical load (i.e., dead load buckling

Table 9 Geometric and material properties for the stiffened ring under external pressure

Frame spacing	L_s	0.6
Mean radius	R	2.488
Shell thickness	e	0.024
Web height	h_w	0.156
Flange width	W_f	0.120
Web thickness	e_w	0.010
Flange thickness	e_f	0.024
Young's modulus	E	200×10^9
Poisson's ratio	ν	0.3

Table 10 Normalized critical buckling pressure for the stiffened cylindrical ring

Mesh	$P_{cr}/P_{cr(ref)}$
300 PRI15 elements	1.01
300 SHB15 elements	1.00
100 HEX20 elements	1.01
100 SHB20 elements	0.99

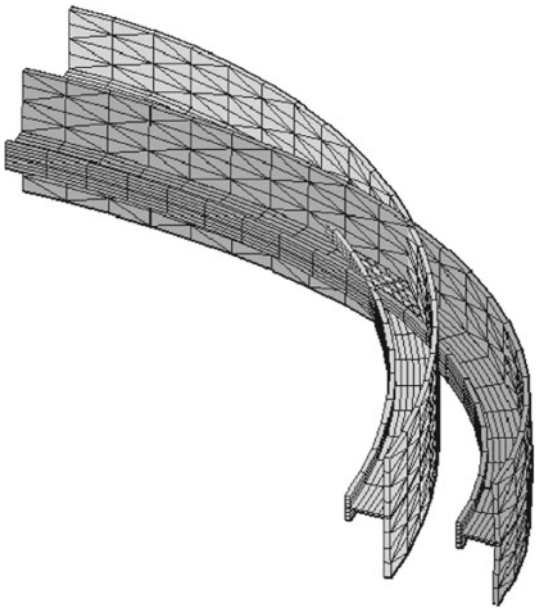

Fig. 7 Illustration of the first Euler buckling mode for the stiffened cylindrical ring under pressure

pressure). A converged solution obtained with a fine mesh of 440 SHB8PS elements is 7.06×10^6, which is in good agreement with previously reported results [40,41]. The obtained results for the critical pressure, after normalization with respect to the reference solution, are reported in Table 10. The corresponding Euler buckling mode is illustrated in Fig. 7.

The results in Table 10 reveal, as also observed previously, that the hexahedral solid–shell SHB20 is more efficient in terms of accuracy and convergence than the prismatic solid–shell SHB15.

4 Conclusions

In this paper, the formulation of two new quadratic solid–shell finite elements, denoted as SHB15 and SHB20, has been given in detail. The SHB15 is a fifteen-node prism and the SHB20 is a twenty-node hexahedron, both having only three translational degrees of freedom per node. The key idea of the derivation is the convenient combination of a 3D approach with some essential shell features. For instance, the integration points are distributed along a special direction, designated as the thickness. The corresponding in-plane reduced integration contributes to alleviate several locking phenomena, while increasing the computational efficiency of the elements. To further enhance the element immunity with regard to shear and thickness-type locking, shell-like behavior is intended by adopting a local physical coordinate system for the specification of the constitutive matrix. In such a local frame, the $x - y$ plane corresponds to the element mid-plane defined by the ζ-coordinate of the considered integration point.

The performance of the resulting solid–shell elements has been assessed, based on the analysis of various linear benchmark problems. The obtained simulation results have been compared to the reference solutions and also to existing conventional 3D solid elements. In all of the benchmark problems tested, the proposed elements showed very good convergence and accuracy. The performance of the SHB15 solid–shell is often found comparable to that of the standard 3D element PRI15; however, the SHB15 admits larger aspect ratios. The SHB20 solid–shell shows remarkable performance both in terms of coarse-mesh accuracy and computational efficiency. Because these elements have only three degrees of freedom per node, they can automatically be combined to mesh arbitrarily complex structural shapes. This possible combination of effective hexahedral and prismatic elements is useful for many applications, and becomes necessary when free mesh generation tools are employed.

Acknowledgments This work has been carried out within a project jointly funded by EDF R&D (French Electricity Company) and CETIM (Technical Center for Mechanical Industries). The authors would like to thank EDF R&D and CETIM for their financial support.

References

1. Hughes TJR (1980) Generalization of selective integration procedures to anisotropic and nonlinear media. Int J Numer Methods Eng 15:1413–1418
2. Flanagan DP, Belytschko T (1981) A uniform strain hexahedron and quadrilateral with orthogonal hourglass control. Int J Numer Methods Eng 17:679–706
3. Belytschko T, Ong JSJ, Liu WK, Kennedy JM (1984) Hourglass control in linear and nonlinear problems. Comput Methods Appl Mech Eng 43:251–276
4. Liu WK, Hu YK, Belytschko T (1994) Multiple-quadrature underintegrated finite elements. Int J Numer Methods Eng 37:3263–3289
5. Koh BC, Kikuchi N (1987) New improved hourglass control for bilinear and trilinear elements in anisotropic linear elasticity. Comput Methods Appl Mech Eng 65:1–46

6. Belytschko T, Bindeman LP (1993) Assumed strain stabilization of the eight node hexahedral element. Comput Methods Appl Mech Eng 105:225–260
7. Stainier L, Ponthot JP (1994) An improved one-point integration method for large strain elastoplastic analysis. Comput Methods Appl Mech Eng 118:163–177
8. Hu YK, Nagy LI (1997) A one-point quadrature eight-node brick element with hourglass control. Comput Struct 65:893–902
9. Masud A, Tham CL, Liu WK (2000) A stabilized 3D co-rotational formulation for geometrically nonlinear analysis of multi-layered composite shells. Comput Mech 26:1–12
10. Bathe KJ, Dvorkin EN (1986) Formulation of general shell elements—the use of mixed interpolation of tensorial components. Int J Numer Methods Eng 22:697–722
11. Onate E, Castro J (1992) Derivation of plate based on assumed shear strain fields. In: Ladevèze P, Zienkiewicz OC (eds) New advances in computational structures mechanics. Elsevier, Amsterdam, pp 237–288
12. Cheung Y, Chen WJ (1992) Refined hybrid method for plane isoparametric element using an orthogonal approach. Comput Struct 42:683–694
13. Boisse P, Gelin JC, Daniel JL (1996) Computation of thin structures at large strains and large rotations using a simple C^0 isoparametric three-node shell element. Comput Struct 58:249–261
14. Ayad R, Dhatt G, Batoz JL (1998) A new hybrid-mixed variational approach for Reissner-Mindlin plates: The MiSP model. Int J Numer Methods Eng 42:1149–1179
15. Chapelle D, Bathe KJ (2003) The finite element analysis of shells—fundamentals. Springer, Berlin
16. Gruttmann F, Wagner W (2004) A stabilized one-point integrated quadrilateral Reissner-Mindlin plate element. Int J Numer Methods Eng 61:2273–2295
17. Cardoso RPR, Yoon JW (2007) One-point quadrature shell elements: a study on convergence and patch tests. Comput Mech 40:871–883
18. Cho C, Park HC, Lee SW (1998) Stability analysis using a geometrically nonlinear assumed strain solid shell element model. Finite Elements Anal Des 29:121–135
19. Hauptmann R, Schweizerhof K (1998) A systematic development of solid-shell element formulations for linear and non-linear analyses employing only displacement degrees of freedom. Int J Numer Methods Eng 42:49–69
20. Sze KY, Yao LQ (2000) A hybrid stress ANS solid-shell element and its generalization for smart structure modelling. Part I—solid-shell element formulation. Int J Numer Methods Eng 48:545–564
21. Abed-Meraim F, Combescure A (2002) SHB8PS—a new adaptive, assumed-strain continuum mechanics shell element for impact analysis. Comput Struct 80:791–803
22. Vu-Quoc L, Tan XG (2003) Optimal solid shells for non-linear analyses of multilayer composites. I. Statics Comput Methods Appl Mech Eng 192:975–1016
23. Chen YI, Wu GY (2004) A mixed 8-node hexahedral element based on the Hu-Washizu principle and the field extrapolation technique. Struct Eng Mech 17:113–140
24. Kim KD, Liu GZ, Han SC (2005) A resultant 8-node solid-shell element for geometrically nonlinear analysis. Comput Mech 35:315–331
25. Klinkel S, Gruttmann F, Wagner W (2006) A robust non-linear solid shell element based on a mixed variational formulation. Comput Methods Appl Mech Eng 195:179–201
26. Reese S (2007) A large deformation solid-shell concept based on reduced integration with hourglass stabilization. Int J Numer Methods Eng 69:1671–1716
27. Zhu YY, Cescotto S (1996) Unified and mixed formulation of the 8-node hexahedral elements by assumed strain method. Comput Methods Appl Mech Eng 129:177–209
28. Wall WA, Bischoff M, Ramm E (2000) A deformation dependent stabilization technique, exemplified by EAS elements at large strains. Comput Methods Appl Mech Eng 188:859–871
29. Puso MA (2000) A highly efficient enhanced assumed strain physically stabilized hexahedral element. Int J Numer Methods Eng 49:1029–1064
30. Soulat D, Cheruet A, Boisse P (2006) Simulation of continuous fibre reinforced thermoplastic forming using a shell finite element with transverse stress. Comput Struct 84:888–903
31. Abed-Meraim F, Combescure A (2009) An improved assumed strain solid-shell element formulation with physical stabilization for geometric nonlinear applications and elastic-plastic stability analysis. Int J Numer Methods Eng 80:1640–1686
32. Trinh VD, Abed-Meraim F, Combescure A (2011) A new assumed strain solid-shell formulation "SHB6" for the six-node prismatic finite element. J Mech Sci Tech 25:2345–2364

33. Trinh VD (2009) Formulation, développement et validation d'éléments finis de type coques volumiques sous-intégrés stabilisés utilisables pour des problèmes à cinématique et comportement non linéaire. PhD Thesis Dissertation, ENSAM Metz
34. Simo JC, Hughes TJR (1986) On the variational foundations of assumed strain methods. J Appl Mech 53:51–54
35. Legay A, Combescure A (2003) Elastoplastic stability analysis of shells using the physically stabilized finite element SHB8PS. Int J Numer Methods Eng 57:1299–1322
36. MacNeal RH, Harder RL (1985) A proposed standard set of problems to test finite element accuracy. Finite Elements Anal Des 1:3–20
37. Belytschko T, Wong BL, Stolarski H (1989) Assumed strain stabilization procedure for the 9-node Lagrange shell element. Int J Numer Methods Eng 28:385–414
38. Timoshenko SP, Gere JM (1966) Théorie de la stabilité élastique, 2nd edn. Dunod. (Theory of elastic stability). McGraw-Hill, New York
39. Brush DO, Almroth BO (1975) Buckling of bars, plates and shells. McGraw-Hill, New York
40. Legay A (2002) Une méthode de calcul efficace pour l'étude paramétrique du flambage non-linéaire de structures tridimensionnelles : application à la fiabilité. PhD Thesis Dissertation, LMT-ENS-Cachan
41. Bourinet JM, Gayton N, Lemaire M, Combescure A (2000) Reliability analysis of stability of shells based on combined finite element and response surface methods. In: Papadrakis M, Samartin A, Onate E (eds) Computational methods for shell and spatial structures. IASS-IACM, Greece